Superradiant Scattering Limit for Arrays of Subwavelength Scatterers

Anna Mikhailovskaya[1,*,†,§] Konstantin Grotov[1,2,‡,§] Dmytro Vovchuk[1] Andrey Machnev,[1]
Dmitry Dobrykh,[1] Roman E. Noskov[1] Konstantin Ladutenko,[2] Pavel Belov,[2] and Pavel Ginzburg[1]

[1]*School of Electrical Engineering, Tel Aviv University, Tel Aviv 69978, Israel*

[2]*School of Physics and Engineering, ITMO University, St. Petersburg 197101, Russia*

Electromagnetic scattering bounds on subwavelength structures play an important role in estimating performance of antennas, radio frequency identification tags, and other wireless communication devices. An appealing approach to increase a scattering cross section is accommodating several spectrally overlapping resonances within a structure. However, numerous fundamental and practical restrictions have been found and led to the formulation of Chu-Harrington, Geyi, and other limits, which provide an upper bound to scattering efficiencies. Here we introduce a two-dimensional array of near-field coupled split-ring resonators and optimize its scattering performance with the aid of a genetic algorithm operating in 19-dimensional space. Experimental realization of the device is demonstrated to surpass the theoretical single-channel limit by a factor of >2, motivating the development of tighter bounds of scattering performance. A superradiant criterion is suggested to compare maximal scattering cross sections with the single-channel dipolar limit multiplied by the number of elements within the array. This empirical criterion, which aims to address performance of subwavelength arrays formed by near-field coupled elements, is found to be rather accurate in application to the superscatterer, reported here. Furthermore, the superradiant bound is empirically verified with a Monte Carlo simulation, collecting statistics on scattering cross sections of a large set of randomly distributed dipoles. The demonstrated flat superscatterer can find use as a passive electromagnetic beacon, making miniature airborne and terrestrial targets radar visible.

I. INTRODUCTION

Scattering cross section characterizes the interaction between incident electromagnetic radiation and a body [1]. It is rather convenient to consider the phenomenon in three different regimes, which are defined by comparing the electromagnetic size of a body with a free-space wavelength. Interactions with large objects can be assessed with ray optics tools, wavelength-comparable geometries require performing full-wave analysis, and subwavelength bodies can be addressed with the Rayleigh approximation. However, structures made of high-dielectric-index materials can be both miniature and resonant. Ceramic elements for the megahertz to gigahertz range [2–9] and semiconductor nanoparticles in the optical domain [10–14] are among representative examples. In many practical cases, antenna devices should be tuned to resonance to achieve better transmitting and receiving performance [15]. Size reduction of devices, operating in low-frequency (kilohertz to megahertz) regimes where implementing

wavelength-comparable designs is not practical, is obtained with lumped impedances loading. While in this case the element can be maintained at a resonance, size reduction implies a significant bandwidth degradation. The Chu-Harrington criterion bounds antenna quality factor (Q-factor) form below, relating it to the device form factor, normalized to an operational wavelength [16]. Being formulated to a dipole resonant condition, the limit can be generalized to include higher-order multipoles. Note that high-Q, a desirable parameter for strengthening light-matter interaction in the optical domain, has negative implications in antenna design, as it degrades operational bandwidths and has a very negative impact on the channel capacity of a wireless communication channel. Hereafter, we concentrate on discussing scattering on subwavelength elements. In this case, multipole expansion is a convenient tool to assess scattering. Each resonant multipole (a scattering channel), being an element of a complete set of basis functions, can contribute to the scattering cross section with $(2\ell + 1)\lambda^2/(2\pi)$, where ℓ is a total angular momentum and λ is a free-space wavelength. $3\lambda^2/(2\pi)$ with $\ell = 1$ is commonly referred to as a dipolar single-channel limit [17].

To bypass the single-channel limit, several resonant multipoles should contribute constructively to the

---
*a.mikhailovskaya@metalab.ifmo.ru

†anna2@mail.tau.ac.il

‡konstantin.grotov@metalab.ifmo.ru

§These authors contributed equally to this work.

scattering. In this case, the structure is called a superscatterer [18–26]. It is worth noting that in geometries lacking a complete rotation symmetry, eigenmodes of a resonator are nontrivially mapped on the far-field multipole expansion of scattering [27,28]. Nevertheless, it is quite intuitive that a superscatterer should accommodate multiple resonances at nearly degenerate frequencies. In this case, a significant near-field accumulation in the vicinity of the structure will emerge, making the design extremely sensitive to material losses of constitutive elements and fabrication tolerances. These aspects are well understood in antenna theory in the context of superdirectivity [29]. To cope with these severe yet solely practical limitations, we have recently introduced structures based on small wire arrays (wire bundles) pinched into a styrofoam holder. This arrangement is almost lossless in the gigahertz frequency range and does not require submillimeter-accurate positioning of elements in respect to each other [30,31].

To reduce the effect of near-field accumulation directly on lossy elements, but nevertheless keep it in the interior of the structure, it is quite appealing to investigate designs made of strongly coupled resonator arrays. The collective response will originate from mode hybridization, which, given a proper design, will lead to superscattering performance. Surpassing the Chu-Harrington dipolar limit, in this case, will emerge quite straightforwardly. The challenge, however, is to formulate a tighter upper bound on the scattering cross section. Here we phenomenologically introduce a superradiant scattering limit, which makes an assessment of structures made of near-field coupled resonators. In this case, the scattering cross section is compared with a single-channel dipolar limit multiplied by the number of elements within the array. In other words, can the coupling improve the scattering performance? It is worth noting that related assessments have been done across different disciplines, e.g., [32,33]. Based on our recent investigations and the current report, it becomes evident that surpassing this limit is quite challenging, if even possible. Appropriate terminology here is a "superradiant scattering limit," as the phenomenon shares similarities with the quantum effect of superradiance [34]. The essence of the latter is the acceleration of the spontaneous decay rate from N quantum systems owing to their mutual phase locking. In our case, the assessment of the total scattering cross section σ_{tot} is as follows:

$$\sigma_{\text{tot}} < \sum_{i=1}^{N} \sigma_i, \tag{1}$$

where σ_i is the scattering cross section of each individual element within the array.

Here we investigate structures based on near-field coupled split-ring resonators (SRRs). Subwavelength SRRs support resonant magnetic dipole modes in the gigahertz spectral range and do not require additional loading

with lumped elements [35–38]. Having enough degrees of freedom to tune electromagnetic parameters, SRRs are promising candidates for superscattering designs.

The manuscript is organized as follows: the superradiant scattering limit is investigated with the aid of discrete dipole approximation, motivating the further development and optimization of structures. Analysis of a single element (SRR) performance and a brief assessment of small arrays is done next. Scattering cross sections of the structures are normalized to the number of elements within the arrays to find an optimal number of elements for further investigations. Given this size (six in our case), a genetic algorithm is set up to optimize the structure further. Experimental assessment of the final design comes next. Discussions on the scattering cross section bounds come before the conclusions.

II. THE SUPERRADIANT LIMIT

To assess the bound, we consider several mutually interacting point scatterers, applying coupled dipole formalism [39]. A dipole moment $(\vec{p}(\vec{r}))$ is proportional to the local electric field $(\vec{E}_{\text{loc}})$ and the particle's polarizability,

$$\vec{p}(\vec{r}) = \varepsilon_0 \overset{\leftrightarrow}{\boldsymbol{\alpha}} \vec{E}_{\text{loc}}(\vec{r}), \tag{2}$$

where $\overset{\leftrightarrow}{\boldsymbol{\alpha}}$ is a polarizability tensor and ε_0 vacuum permittivity. For the sake of simplicity, magnetic and magnetoelectric interactions are ignored [40,41]. The N dipoles problem is then formulated within $3N$ linear equations taking into account the vectorial nature of the problem,

$$\vec{p}_i(\vec{r}_i) = \varepsilon_0 \overset{\leftrightarrow}{\boldsymbol{\alpha}_i} \left[\overrightarrow{E_0}(\vec{r}_i) + \sum_{n \neq i}^{N} \overset{\leftrightarrow}{\mathbf{G}}(r_i, r_n) \vec{p}_n(\vec{r}_n) \right],$$
$$i = 1, \dots, N, \tag{3}$$

where $\overset{\leftrightarrow}{\mathbf{G}}$ is the Green tensor of the single dipole and $\overrightarrow{E_0}$ is the incident field. This set of equations can be solved by a matrix inversion, which allows calculating dipole moments self-consistently. Then, the extinction cross section can be obtained from the optical theorem,

$$\sigma_{\text{ext}} = \frac{4\pi k}{|\vec{E}_0|^2} \sum_{i=1}^{N} \text{Im}(\overrightarrow{E_0}^*(\vec{r}_i) \cdot \vec{p}_i(\vec{r}_i)), \tag{4}$$

where $k = 2\pi/\lambda$ is the wave number and the incident field amplitude variation on the array is neglected (plane-wave excitation is assumed).

For assessing the superradiant limit, the following numerical experiment is performed: N resonant point dipoles are randomly distributed in a subwavelength cubic volume with side of $\lambda/5$. The dipoles are not allowed to

approach each other at a distance smaller than $\lambda/40$. The dipoles are isotropic, lossless, and identical with polarizability of a subwavelength sphere made of a lossless Drude material. Relative permittivity ($\varepsilon_r = -2$) is the resonance condition. Radiation corrections are included in the polarizability model [42]. This numerical setup is rather arbitrary and solely serves for assessing possible extinction cross sections statistically.

Figure 1 shows the probability distributions of the normalized cross sections for different numbers of dipoles, where N is indicated in the figure. The horizontal axis is $\sigma_{\text{ext}}^{\text{total}}/N \cdot \sigma_{\text{ext}}^{\text{single}}$, where $\sigma_{\text{ext}}^{\text{single}}$ is the maximal extinction of a single resonant dipole. $\sigma_{\text{ext}}^{\text{total}}$ is the maximal extinction of the array. Note that the resonance of the coupled system and the single dipole can be shifted in frequency. The probability distribution is calculated upon assessing 1000 random realizations (uniform distribution in the volume, no correlation between the dipole locations). The superradiant limit is 1 on the horizontal axis. Figs. 1(a)

and 1(b) differ by dipole polarizability. "Strong" corresponds to the lossless material's dipole polarizability at its resonance, and "weak" to the same value divided by 10. The following observations can be made: (i) none of the realizations break the limit statistically; (ii) increasing the number of dipoles in the volume shifts the distribution to the left, i.e., it moves away from the limit (on average). It is worth noting that the local field within the array is extremely nonuniform, making effective-medium theories [43] barely applicable. Several realizations from the sample space appear in Appendix. Those correspond to the maximal, mean, and minimal scattering that are observed. It is worth noting that the realizations have no pronounced spatial arrangement and, as a result, are hardly predictable. It is quite obvious that probability distributions in the weak polarizability regime, implying minor dipole-dipole coupling, peak in the vicinity of 1. Increasing the number of dipoles in the box results in the reduction of the scattering cross section on average. Note that the overall scattering cross sections in the strong polarizability regime are higher than in the weak case, which increases the challenge in finding a proper configuration.

This analysis demonstrates that approaching the limit with a large number of dipoles without extensive optimization is challenging. Furthermore, it is impossible to draw a conclusion on when the limit can be overcome. The objective of the next sections is to assess this limit from the practical standpoint. Magnetic dipoles instead of electric ones are used.

III. THE ELECTROMAGNETIC DESIGN AND STRUCTURE'S OPTIMIZATION

Prior to analyzing arrays, performance of single elements is briefly surveyed. Electromagnetic modeling is performed in CST Microwave Studio Suite, Frequency Domain Solver. The number of mesh cells is approximately $(1.5–2) \times 10^5$ for all models. For the basic element we choose a double circle split-ring resonator (CSRR), as it has a smaller footprint, higher Q-factor, and symmetrized response compared with a single SRR. The CSRR can be tuned to a resonance in the gigahertz-spectral range without a need to introduce additional lumped impedances. CSRRs are implemented by etching copper strips on a dielectric substrate [Isola IS680 AG338, with $\varepsilon_r \approx 3.338$ and $\tan(\delta) = 0.0026$ being the relative permittivity and loss tangent]. The inner and outer radii of the ring are $r_{\text{in}} = 1.9$ mm and $r_{\text{out}} = 3.5$ mm, respectively. The metal strip's width is 1 mm and thickness 35 μm, with the gap between the inner and outer rings being 0.4 mm. The upper split in the outer ring and the symmetric split in the inner ring have the same width of 1 mm. The single CSRR on a substrate is tuned to resonate at 5.2 GHz (magnetic dipole dominates the interaction), with the Q-factor of 61.
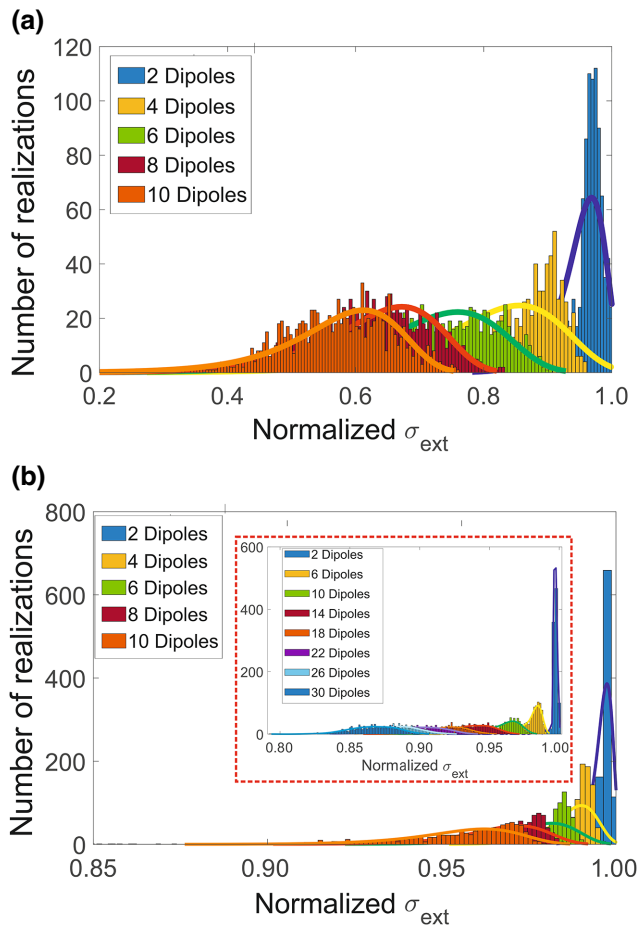

FIG. 1.   Assessment of the superradiant scattering limit. Probability distribution on the normalized extinction cross section ($\sigma_{\text{ext}}^{\text{total}}/N\sigma_{\text{ext}}^{\text{single}}$) for N coupled dipoles in a subwavelength volume. (a) Strong polarizability case with resonant lossless dipoles. (b) Weak polarizability at 1/10 of the previous case.

(a)

(b)

$$\sigma_{\rm tot}/{\rm max}(\sigma_{\rm tot}^{\rm Single\ CSRR})$$
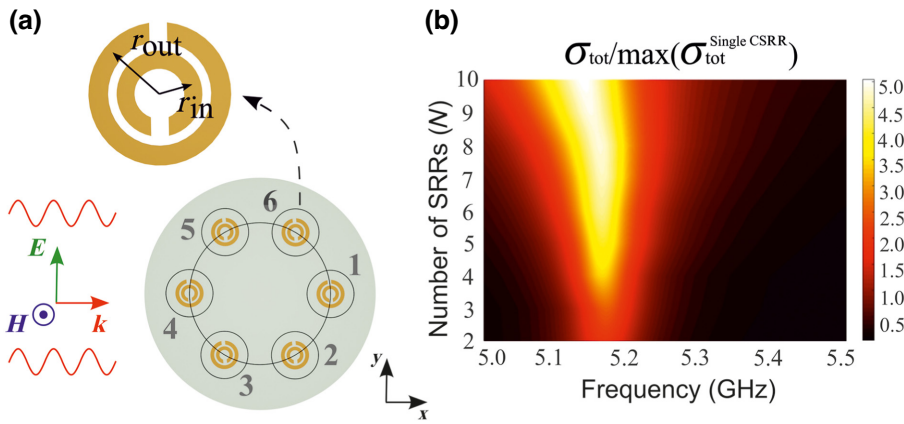
FIG. 2. (a) Schematics of a single CSRR, array, and the incident plane wave. (b) Numerical analysis: the total scattering cross section normalized to the maximal total scattering of a single CSRR as a function of frequency and the number of elements within the array.

At the next stage, the number of elements within the array is chosen. Figure 2(b) is a color map showing the total normalized scattering cross section as a function of frequency and number of elements within the array (2–10 element arrays are investigated). As the last variable is discrete, a linear interpolation is made. Horizontal cuts correspond to the normalized scattering spectra. The normalization is made by dividing the values by the scattering cross section of a single CSRR, $\sigma_{\rm tot}/{\rm max}(\sigma_{\rm tot}^{\rm single\ CSRR})$. In all cases, the elements are equally distributed on a circle with $r = 25$ mm radius. This number is quite arbitrary; nevertheless it is chosen to keep the structure electrically small, e.g., $2r/\lambda < 1$. In these studies, all the CSRRs are mutually aligned [their gaps are kept parallel, as it appears in Fig. 2(a)]. While the single-channel dipolar ($\ell = 1$) limit for an ideal CSRR is $3\lambda^2/(2\pi) \approx 15.9$ cm^2, in the presence of a lossy substrate the practically achievable value is approximately 11 cm^2 (at 5.2 GHz). The color map in Fig. 2(b) clearly indicates that the six-element array is the best candidate for further investigating the superscattering effect. $\sigma_{\rm tot}/{\rm max}(\sigma_{\rm tot}^{\rm single\ CSRR})$ approaches its maximum for six CSRRs and almost saturates for larger arrays. Relying on this observation, we concentrate on this "magic" number hereafter; nevertheless, any other configuration can be chosen as a starting point. Note that the saturation effect has nothing to do with statistical distributions in Fig. 1, as it relates to specific preoptimized realizations.

While the previously investigated structure is rather symmetric, symmetry breaking can lead to a significant improvement of certain electromagnetic parameters. A good example is photonic crystal cavities, where a miniature displacement of holes around a defect was found to boost Q-factors by orders of magnitude [44,45].

Scattering-cross-section maximization is an optimization problem in a multiple variable space. A choice of an optimization algorithm is always a subject to several trade-offs, compromising between computational efforts and the reliability of a solution. An evolutionary algorithm (particle swarm optimization is used here) starts its initial iteration with a set of random vectors (individuals). There are well-understood conditions where this algorithm converges to a global extremum with a probability of 1 [46]. Nevertheless, it is quite difficult to fulfill all the requirements to ensure the convergence, which then comes at the expense of computational efforts. Consequently, in many practical applications, the possible heuristic proof of a global minimum is waived in a favor of resource reduction [47,48]. Inverse design using deep learning is another approach that can be employed for the optimization (e.g., Refs. [49,50]). However, machine learning models, e.g., deep neural networks, require a large amount of training data and are less useful for designs discussed here.

Evolutionary algorithms apply basic provisions adopted from biological evolution theory. Main steps consist of selection, mutation, and crossover. A random initial population evolves in accordance with the selection rules (which depend on the fitness function) and only the best individuals reach the next iteration of the algorithm. Since being considered in 1956 [51], evolutionary methods are extensively used nowadays in various fields of physics. Antenna design [52,53], including the famous NASA-evolved antenna [54], two-dimensional materials design [55–57], development of reflective and absorbing structures [58] and metasurfaces [59,60], design of artificial magnetic metamaterials [61], and plasmonic nanoparticles [62] are among the examples. Hereafter, we use a particle swarm optimization algorithm, where the following parameters are chosen to form the search space: the radius R of the circle on which the CSRRs are initially located, the angle of rotation α_i of each CSRR relative to its center, and the position of the element in the neighborhood of the starting point (this parameter is chosen as $\delta = R/3$ to prevent a potential geometrical overlap between the array elements). For convenience, the position of the ith ring is given in polar coordinates (ρ_i, ϕ_i). Thus, the optimization vector of parameters contains 19 components. The radius (R) is varied from 10 to 60 mm, the rotation angles (α_i) of each CSRR from $-\pi$ to π, ρ_i from 0 to 5 mm, and ϕ_i from $-\pi$ to π. Zero angle corresponds to the y-axis direction.
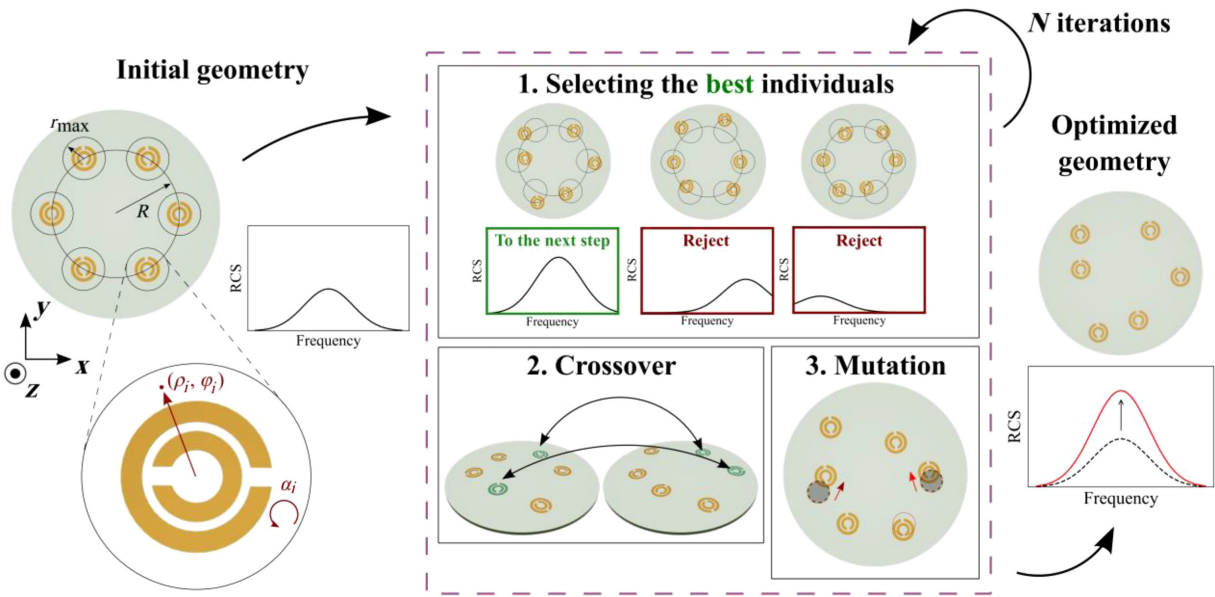
FIG. 3. Scheme of the optimization algorithm.

The final set of parameters obtained with the optimizer are summarized in Appendix.

Figure 3 is a schematic representation the optimization algorithm flow. At the beginning, a population of N individuals (random vectors of parameters) is formed. Each of the individuals corresponds to a certain design, which is modeled in CST Microwave Studio. The excitation is kept the same—a plane wave propagates along the x axis with the magnetic field polarized along z axis. The maximal scattering cross section is constrained to appear in the 5–6 GHz interval. Setting a hard restriction on the resonant frequency might cause conversion issues and, hence, this parameter is better being loosely defined. After an integration with the direct solver (evaluation of the electromagnetic problem with CST), the algorithm singles out optimum individuals of the population, which proceed to the stage of crossover and mutation. As a result of the crossover, a new generation of individuals is created. Further, the mutation operator is applied to the resulting

new generation, the purpose of which is to add a small perturbation to the components of the vectors of the new population (the implementation of the mutation operator may also differ from the implementation of the algorithm). At the end of each step of the algorithm, the scattering spectra of new individuals are calculated, and new best representatives of the population are selected. This process is repeated $N_{\text{iterations}}$ times and after exiting the algorithm, the best individual is obtained—the design that corresponds to the best-found scattering spectrum.

The numerical experiment is carried out with $N_{\text{iterations}} = 1000$. The runtime on 512 GB RAM 3.3 GHz, is 2000 min (about 2 min for a single iteration). The same machine is used to run the algorithm and CST.

Our final superscatterer design is shown in Fig. 4(a). Parameters of the structure are summarized in Table I (Appendix). Figure 4(b) shows the comparison of scattering cross sections of a single CSRR, unoptimized array, and the result of the genetic algorithm. The growth
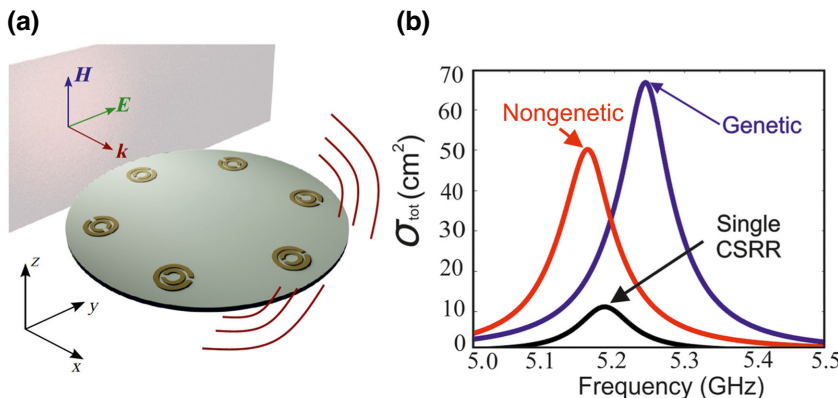

FIG. 4. (a) Schematics of a flat superscatterer. Six CSRRs are distributed on a substrate (Isola IS680 AG338). Illumination is a plane wave, propagating along the x axis and polarized along the y axis. (b) Scattering cross section spectra of the superscatterer (genetic design), blue solid line; six equidistantly distributed SRRs in a circle, red solid line; and a single CSRR, black solid line.

of the scattering peak can be clearly seen with the genetic design prevailing the unoptimized counterpart by a factor of 1.4. The resonant frequencies of all three structures differ slightly from each other as a result of relaxing this variable in the optimization.

To reveal the device operation, multipolar expansion of the scattering spectra is done. In this case, the finite-element method (COMSOL Multiphysics) is used. The multipole expansion of the scattering cross section, i.e., the sum of the contributions from different multipole moments up to the third order is given by the formula for Cartesian multipoles [63–65],

$$
\sigma_{\text{sca}}^{\text{tot}} = \sigma_{\text{sca}}^{p} + \sigma_{\text{sca}}^{m} + \sigma_{\text{sca}}^{Q^e} + \sigma_{\text{sca}}^{Q^m} + \sigma_{\text{sca}}^{O^e} + \sigma_{\text{sca}}^{O^m}
$$

$$
\approx \frac{k^4}{6\pi\varepsilon_0^2|E_0^2|}|p_j|^2 + \frac{k^4\varepsilon_h}{6\pi\varepsilon_0^2c^2|E_0^2|}|m_j|^2
$$

$$
+ \frac{k^6}{80\pi\varepsilon_0^2|E_0^2|}|Q_{jk}^e|^2 + \frac{k^6\varepsilon_h^2}{80\pi\varepsilon_0^2c^2|E_0^2|}|Q_{jk}^m|^2
$$

$$
+ \frac{k^8\varepsilon_h^2}{1890\pi\varepsilon_0^2|E_0^2|}|O_{jkl}^e|^2 + \frac{k^8\varepsilon_h^3}{1890\pi\varepsilon_0^2c^2|E_0^2|}|O_{jkl}^m|^2,
$$

$$(5)$$

where $|E_0|$ is the electric field amplitude of the incident plane wave, k is the wavenumber, c is the speed of light, ε_h is the permittivity of the host media (air in our case), ε_0 is the permittivity of vacuum, p_j and m_j are the electric and magnetic dipole moments (ED and MD), (Q_{jk}^e) and (Q_{jk}^m) are the electric and magnetic quadrupoles (EQ and MQ), and (O_{jkl}^e) and (O_{jkl}^m) electric and magnetic octupoles (EO and MO).

Figure 5 summarizes the expansion results for the nonoptimized array and for the array obtained by the genetic algorithm. Recall that the nonoptimized array is nevertheless tuned to its resonance, exhibiting high scattering performance. While in both of the cases, multipole contributions have overlapping resonances, the genetic design leads to a better collocation and, remarkably, brings a MD resonance, which is missing in the initial array (dashed brown line in Fig. 5). Overall, the multipole series reproduce the peak; nevertheless, the exact conversion is not

obtained. The conclusion here is that higher-order multipoles in the series are missing. Including them explicitly is a rather complex task, as mathematic formulation becomes involved. It is worth noting that the lack of conversions in electrically small structures is extremely rare and, typically, several multipoles describe the interaction quite accurately. Constructive interference of six multipoles in our structure becomes evident.

IV. EXPERIMENTAL MEASUREMENTS

The sample consisting of six CSRRs is manufactured by chemical etching. Isola IS680 AG338 [$\varepsilon_r = 3.338$, $\tan(\delta) = 0.0026$] is used as a low-loss substrate. The thickness of the dielectric support is 0.2 mm, while the thickness of the copper layer is around 35 μm. These parameters are used to reduce the influence of the substrate on the array's performance. The CSRRs are arranged according to the layout provided by the algorithm. The fabrication process is optimized to provide high-quality samples with submillimeter precision in all the parameters, though without using clean-room facilities. The experimental sample is shown in the inset of Fig. 6(b).

Experimental spectra are shown in Fig. 6(b). Several angles (see captions) of incidence are considered. The sample is rotated around its axis [see Fig. 6(a)], while the magnetic field is always polarized along the CSRRs' normal. The optical theorem is used to evaluate the total scattering cross section. The angular dependence here is relatively weak, making the device attractive from an application point of view, as accurate alignment is not required. The black dashed line shows the scattering spectrum of a single CSRR. Its peak is 5 times smaller than the maximal scattering cross section of the array.

V. DISCUSSION

After demonstrating the structure's performance, assessing fundamental limits is made possible.

A. Single-channel limit

The single-channel limit is defined in the Introduction. For this structure it is 17.9 cm^2 (at 4.9 GHz).
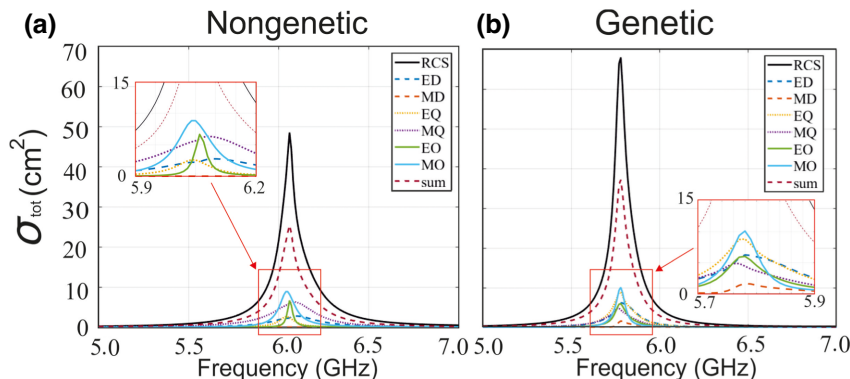

FIG. 5. Multipole expansion of the scattering cross section of (a) a nonoptimized array and (b) array obtained with the genetic algorithm. Abbreviations appear in captions and are explained in the main text.
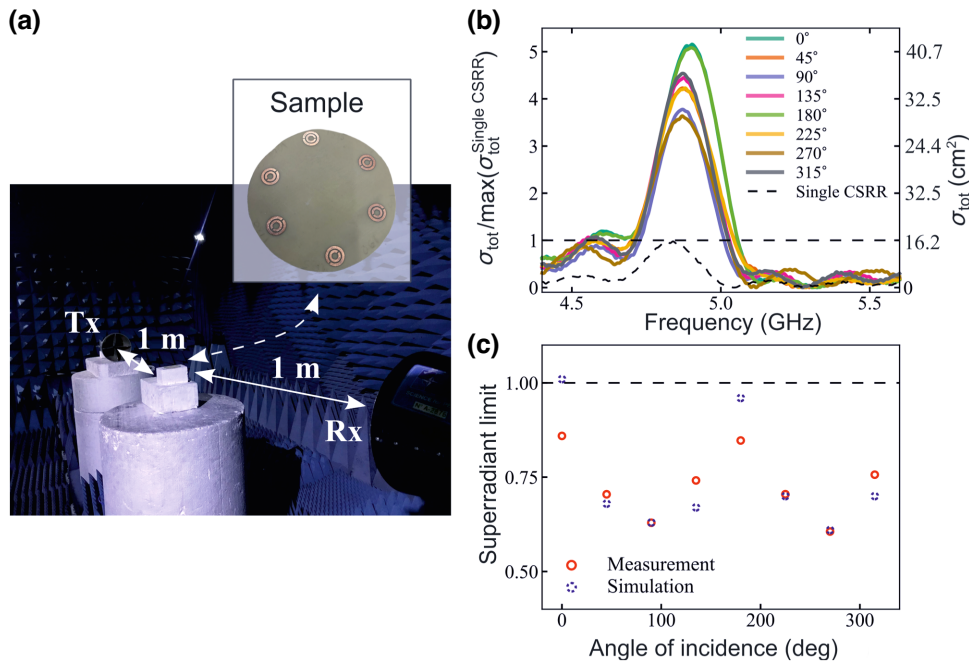
FIG. 6. (a) Experimental setup to measure scattering cross section. Inset shows the sample. (b) Experimental total scattering cross section spectra for different angles of incidence (in captions). (c) Superradiant limit, experimental and numerical data. Different angles of incidence are considered. Tx refers to transmit antenna; Rx refers to receive antenna.

Note that the single CSRR with the maximal scattering of 8.146 cm^2 does not reach this limit because of losses. Our structure is found to beat the single channel limit by around 2.17.

B. Superradiant scattering limit

Our newly introduced limit is assessed next, considering $\sigma_{tot}^{structure}/(N\sigma_{tot}^{single\ CSRR})$, where $N = 6$. This assessment allows underlining of the impact of near-field coupling on the total scattering. Figure 6(c) demonstrates the limit for different angles of incidence. The maximum is obtained for 0°, for which the structure is initially optimized. It is worth noting that the numerical analysis predicts overcoming the superradiant limit by a small fraction, while the experimental results drop below this value. This is a rather good indication that the empirical formulation of this bound is tight and difficult to bypass. The experimental sample is rather sensitive to many factors including substrate losses, fabrication accuracy, and the surrounding environment. While the chemical etching is made quite accurately, the substrate permittivity might have fluctuations, as well as the copper layer. All these aspects lead to deviations between the theoretical predictions and practical results.

VI. CONCLUSION

The design and experimental realization of the superscatterer based on a SRR array is demonstrated. A genetic algorithm, optimizing 19 independent degrees of freedom, is implemented to design spectral overlap of eight multipolar contributions at the same frequency. The experimental sample is shown to surpass the single-channel limit by a factor of 2.17 and motivates the development of new more practical bounds to assess scattering performance of structures made of near-field coupled elements. A superradiant bound is formulated, suggesting a comparison of the maximal scattering cross section with a single-channel dipolar limit multiplied by the number of elements within the array. The bound is empirically assessed with the aid of Monte Carlo simulation. We perform a numerical experiment, calculating scattering cross sections of a large set of randomly distributed point dipoles placed within a subwavelength volume. Any realization succeeds to overcome the superradiant bound, suggesting its accuracy, albeit on a statistical basis. While quite a few physical limits in electromagnetism have been developed [66], the superradiant limit is quite appealing owing to its application simplicity.

The designed six-element array succeeds in overcoming this bound by a small fraction in theory, while the experimental values are found below the limit. These results indicate that this new assessment sets a rather tight limitation and promotes its further use in the field of superscattering.

The demonstrated superscatterer is two-dimensional and it is implemented on a thin flexible lightweight substrate. Similar designs can find a use in many practical applications, including electromagnetic passive beacons, alignment marks for indoor navigation, radar chaff, and many others.

APPENDIX

Figures 7 and 8 demonstrate several realizations from the sample space. The realization correspond to the distribution tails and the mean, as indicated in the figures. Figure 7 corresponds to Fig. 1(a), File Fig. 8 is related to Fig. 1(b).

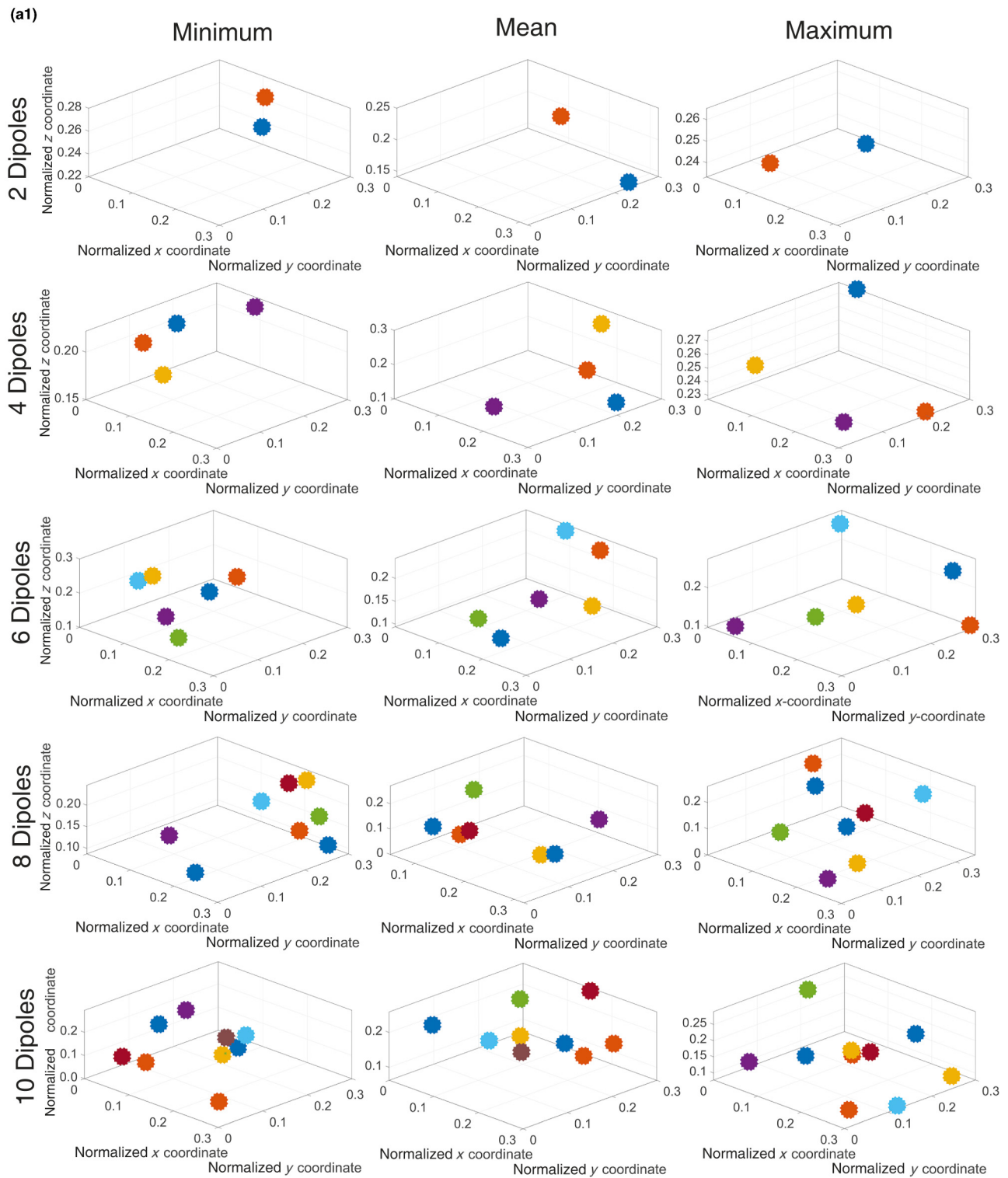Table I summarizes all the design parameters of the optimized superscatterer.

FIG. 7.　Minimum, mean, and maximum realizations of the dipole arrangement from the sample space for the strong polarizability case.
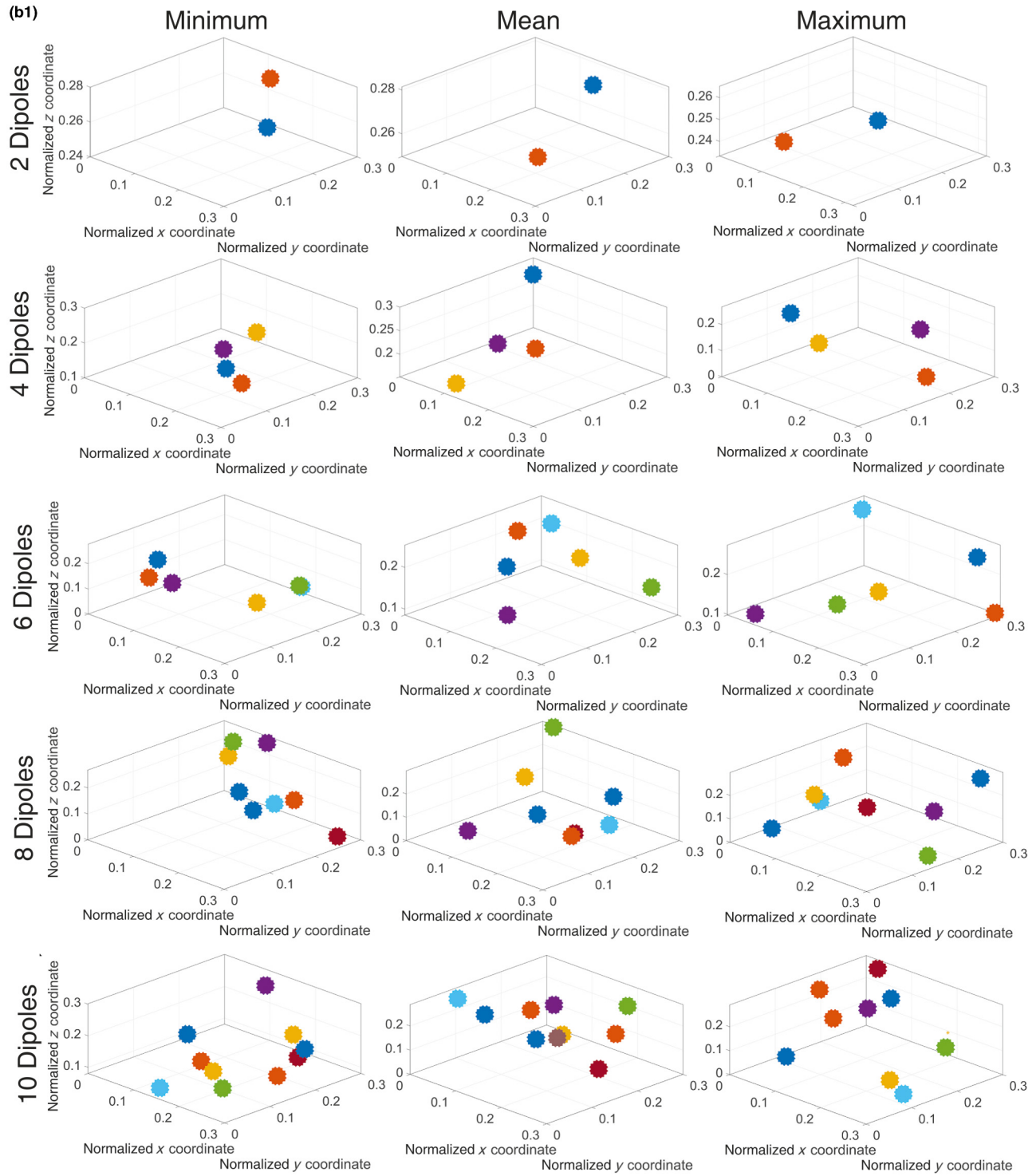
FIG. 8.   Minimum, mean, and maximum realizations of the dipole arrangement from the sample space for the weak polarizability case.

TABLE I. Final parameters of the optimization result.

Parameter	SRR number	Value
α_i	1	86.5°
	2	25.5°
	3	−171.4°
	4	101.9°
	5	−138.5°
	6	−37.2°
ρ_i	1	2.93 mm
	2	0.48 mm
	3	3.49 mm
	4	2.15 mm
	5	0.03 mm
	6	1.69 mm
ϕ_i	1	114.7°
	2	−165.3°
	3	123.4°
	4	−122.3°
	5	−103.9°
	6	86°
R		25 mm

[1] J. D. Jackson, *Classical Electrodynamics*, 3rd ed. (Wiley, New York, 1998).

[2] A. Mikhailovskaya, I. Yusupov, D. Dobrykh, S. Krasikov, D. Shakirova, A. Bogdanov, D. Filonov, and P. Ginzburg, Omnidirectional miniature RFID tag, Appl. Phys. Lett. **119**, 033503 (2021).

[3] D. Dobrykh, I. Yusupov, S. Krasikov, A. Mikhailovskaya, D. Shakirova, A. A. Bogdanov, A. Slobozhanyuk, D. Filonov, and P. Ginzburg, Long-range miniaturized ceramic RFID tags, IEEE Trans. Antennas Propag. **69**, 3125 (2021).

[4] K. Baryshnikova, D. Filonov, C. Simovski, A. Evlyukhin, A. Kadochkin, E. Nenasheva, P. Ginzburg, and A. S. Shalin, Giant magnetoelectric field separation via anapole-type states in high-index dielectric structures, Phys. Rev. B **98**, 165419 (2018).

[5] P. Kapitanova, V. V. Soshenko, V. V. Vorobyov, D. Dobrykh, S. V. Bolshedvorskii, V. N. Sorokin, and A. V. Akimov, 3D uniform manipulation of NV centers in diamond using a dielectric resonator antenna, JETP Lett. **108**, 588 (2018).

[6] M. T. Sebastian, R. Ubic, and H. Jantunen, Low-loss dielectric ceramic materials and their properties, Int. Mater. Rev. **60**, 392 (2015).

[7] A. Petosa, *Dielectric Resonator Antenna Handbook* (Artech House, Inc., Norwood, USA, 2007), pp. 336.

[8] I. Yusupov, D. Filonov, A. Bogdanov, P. Ginzburg, M. V. Rybin, and A. Slobozhanyuk, Chipless wireless temperature sensor based on quasi-BIC resonance, Appl. Phys. Lett. **119**, 193504 (2021).

[9] S. Keyrouz and D. Caratelli, Dielectric resonator antennas: basic concepts, design guidelines, and recent developments at millimeter-wave frequencies, Int. J. Antennas Propag. **2016**, 21 (2016).

[10] S. Jahani and Z. Jacob, All-dielectric metamaterials, Nat. Nanotechnol. **11**, 23 (2016).

[11] A. E. Krasnok, A. B. Evlyukhin, B. N. Chichkov, D. G. Baranov, D. A. Zuev, O. V. Kotov, and S. I. Lepeshov, All-dielectric nanophotonics: The quest for better materials and fabrication techniques, Optica **4**, 814 (2017).

[12] A. I. Kuznetsov, A. E. Miroshnichenko, Y. H. Fu, J. Zhang, and B. Lukyanchukl, Magnetic light, Sci. Rep. **2**, 1 (2012).

[13] A. I. Kuznetsov, A. E. Miroshnichenko, M. L. Brongersma, Y. S. Kivshar, and B. Luk'yanchuk, Optically resonant dielectric nanostructures, Science **354**, 846 (2016).

[14] D. Permyakov, I. Sinev, D. Markovich, P. Ginzburg, A. Samusev, P. Belov, V. Valuckas, A. I. Kuznetsov, B. S. Luk'yanchuk, A. E. Miroshnichenko, D. N. Neshev, and Y. S. Kivshar, Probing magnetic and electric optical responses of silicon nanoparticles, Appl. Phys. Lett. **106**, 171110 (2015).

[15] C. A. Balanis, *Antenna Theory: Analysis and Design*, 3rd ed. (Wiley-Interscience, Hoboken, New Jersey, 2005).

[16] R. F. Harrington, On the gain and beamwidth of directional antennas, IRE Trans. Antennas Propag. **AP-6**, 219 (1958).

[17] Z. Ruan and S. Fan, Superscattering of Light from Subwavelength Nanostructures, Phys. Rev. Lett. **105**, 013901 (2010).

[18] V. I. Shcherbinin, V. I. Fesenko, T. I. Tkachova, and V. R. Tuz, Superscattering from Subwavelength Corrugated Cylinders, Phys. Rev. Appl. **13**, 024081 (2020).

[19] C. Qian, X. Lin, Y. Yang, X. Xiong, H. Wang, E. Li, I. Kaminer, B. Zhang, and H. Chen, Experimental Observation of Superscattering, Phys. Rev. Lett. **122**, 063901 (2019).

[20] Z. Ruan and S. Fan, Design of subwavelength superscattering nanospheres, Appl. Phys. Lett. **98**, 043101 (2011).

[21] T. Lee, T. Nomura, P. Schmalenberg, E. M. Dede, and H. Iizuka, Directional Acoustic Superscattering by Coupled Resonators, Phys. Rev. Appl. **12**, 054059 (2019).

[22] C. Qian, X. Lin, Y. Yang, F. Gao, Y. Shen, J. Lopez, I. Kaminer, B. Zhang, E. Li, M. Soljačić, and H. Chen, Multifrequency superscattering from subwavelength hyperbolic structures, ACS Photonics **5**, 1506 (2018).

[23] A. Mirzaei, A. E. Miroshnichenko, I. V. Shadrivov, and Y. S. Kivshar, Superscattering of light optimized by a genetic algorithm, Appl. Phys. Lett. **105**, 011109 (2014).

[24] D. Vovchuk, S. Kosulnikov, R. E. Noskov, and P. Ginzburg, Wire resonator as a broadband huygens superscatterer, Phys. Rev. B **102**, 094304 (2020).

[25] S. Kosulnikov, D. Filonov, A. Boag, and P. Ginzburg, Volumetric metamaterials versus impedance surfaces in scattering applications, Sci. Rep. **11**, 9571 (2021).

[26] D. Filonov, A. Shmidt, A. Boag, and P. Ginzburg, Artificial localized magnon resonances in subwavelength metaparticles, Appl. Phys. Lett. **113**, 123505 (2018).

[27] D. Dobrykh, D. Shakirova, S. Krasikov, A. Mikhailovskaya, I. Yusupov, A. Slobozhanyuk, K. Ladutenko, D. Filonov, A. Bogdanov, and P. Ginzburg, Multipole engineering for enhanced backscattering modulation, Phys. Rev. B **102**, 195129 (2020).

[28] S. Krasikov, M. Odit, D. Dobrykh, I. Yusupov, A. Mikhailovskaya, D. Shakirova, A. Shcherbakov, A.

Slobozhanyuk, P. Ginzburg, D. Filonov, and A. Bogdanov, Multipolar Engineering of Subwavelength Dielectric Particles for Scattering Enhancement, Phys. Rev. Appl. **15,** 024052 (2021).

[29] R. C. Hansen, *Electrically Small, Superdirective, and Superconducting Antennas* (John Wiley & Sons, Hoboken, New Jersey, 2006), pp. 168.

[30] S. Kosulnikov, D. Vovchuk, R. E. Noskov, A. Machnev, V. Kozlov, K. Grotov, K. Ladutenko, P. Belov, and P. Ginzburg, Circular wire-bundle superscatterer, J. Quant. Spectrosc. Radiat. Transfer **279,** 108065 (2022).

[31] K. Grotov, D. Vovchuk, S. Kosulnikov, I. Gorbenko, L. Shaposhnikov, K. Ladutenko, P. Belov, and P. Ginzburg, Genetically designed wire bundle super-scatterers, IEEE Trans. Antennas Propag. **1,** 1 (2022).

[32] M. A. Kuntman, E. Kuntman, J. Sancho-Parramon, and O. Arteaga, Light scattering by coupled oriented dipoles: decomposition of the scattering matrix, Phys. Rev. B **98,** 045410 (2018).

[33] F. Andreoli, M. J. Gullans, A. A. High, A. Browaeys, and D. E. Chang, Maximum Refractive Index of an Atomic Medium, Phys. Rev. X **11,** 011026 (2021).

[34] R. H. Dicke, P. Physical, and I. Aboratory, Coherence in Spontaneous Radiation Processes, Phys. Rev. **93,** 99 (1954).

[35] P. Gay-Balmaz and O. J. F. Martin, Electromagnetic resonances in individual and coupled split-ring resonators, J. Appl. Phys. **92,** 2929 (2002).

[36] B. Sauviac, C. R. Simovski, and S. A. Tretyakov, Double split-ring resonators: analytical modeling and numerical simulations, Electromagnetics **24,** 317 (2004).

[37] J. D. Baena, L. Jelinek, R. Marqués, and M. Silveirinha, Unified homogenization theory for magnetoinductive and electromagnetic waves in split-ring metamaterials, Phys. Rev. A **78,** 013842 (2008).

[38] Filippo Capolino, *Applications of Metamaterials* (CRC Press, Boca Raton, FL, 2017).

[39] B. Novotny and L. Hecht, *Propagation and Focusing of Optical Fields, in Principles of Nano-Optics* (Cambridge University Press, New York, 2012), pp. 45–85.

[40] Y. Ra'di and S. A. Tretyakov, Corrigendum: Balanced and optimal bianisotropic particles: Maximizing power extracted from electromagnetic fields, New J. Phys. **15,** 129501 (2013).

[41] V. Kozlov, D. Filonov, A. S. Shalin, B. Z. Steinberg, and P. Ginzburg, Asymmetric backscattering from the hybrid magneto-electric meta particle, Appl. Phys. Lett. **109,** 203503 (2016).

[42] A. Wokaun, J. P. Gordon, and P. F. Liao, Radiation Damping in Surface-Enhanced Raman Scattering, Phys. Rev. Lett. **48,** 957 (1982).

[43] A. H. Sihvola and Institution of Electrical Engineers, *Electromagnetic Mixing Formulas and Applications* (Institution of Electrical Engineers, London, UK, 1999).

[44] *Roadmap on Photonic Crystals*, edited by S. Noda and T. Baba (Springer, Boston, MA, USA, 2003).

[45] Y. Akahane, T. Asano, B. S. Song, and S. Noda, High-Q photonic nanocavity in a two-dimensional photonic crystal, Nature **425,** 944 (2003).

[46] W. Qian and M. Li, Convergence analysis of standard particle swarm optimization algorithm and its improvement, Soft Comput. **22,** 4047 (2018).

[47] S. Jafar-Zanjani, S. Inampudi, and H. Mosallaei, Adaptive genetic algorithm for optical metasurfaces design, Sci. Rep. **8,** 11040 (2018).

[48] Y. Fan, Y. Xu, M. Qiu, W. Jin, L. Zhang, E. Y. Lam, D. P. Tsai, and D. Lei, Phase-controlled metasurface design via optimized genetic algorithm, Nanophotonics **9,** 3931 (2020).

[49] Z. Li, R. Pestourie, Z. Lin, S. G. Johnson, and F. Capasso, Empowering metasurfaces with inverse design: Principles and applications, ACS Photonics **9,** 2178 (2022).

[50] S. Krasikov, A. Tranter, A. Bogdanov, and Y. Kivshar, Intelligent metaphotonics empowered by machine learning, Opto-Electron. Adv. **5,** 210147 (2022).

[51] N. A. Barricelli, A "chromosomic" recombination theory for multiplicity reactivation in phages, Acta Biotheor. **11,** 107 (1956).

[52] Q. Xu, S. Zeng, F. Zhao, R. Jiao, and C. Li, On formulating and designing antenna arrays by evolutionary algorithms, IEEE Trans. Antennas Propag. **69,** 1118 (2021).

[53] T. Feichtner, O. Selig, M. Kiunke, and B. Hecht, Evolutionary Optimization of Optical Antennas, Phys. Rev. Lett. **109,** 127701 (2012).

[54] G. S. Hornby, A. Globus, D. S. Linden, and J. D. Lohn, in *Collection of Technical Papers - Space 2006 Conference* (2006), Vol. 1, pp. 445.

[55] S. Preble, M. Lipson, and H. Lipson, Two-dimensional photonic crystals designed by evolutionary algorithms, Appl. Phys. Lett. **86,** 061111 (2005).

[56] B. C. Revard, W. W. Tipton, A. Yesypenko, and R. G. Hennig, Grand-Canonical Evolutionary Algorithm for the Prediction of Two-Dimensional Materials, Phys. Rev. B **93,** 054117 (2016).

[57] A. J. Lew and M. J. Buehler, A deep learning augmented genetic algorithm approach to polycrystalline 2D material fracture discovery and design, Appl. Phys. Rev. **8,** 041414 (2021).

[58] H. Cai, Y. Sun, J. Liu, and X. Wang, Genetic algorithm optimization for highly efficient solar thermal absorber based on optical metamaterials, J. Quant. Spectrosc. Radiat. Transfer **271,** 107712 (2021).

[59] M. Ohira, H. Deguchi, M. Tsuji, and H. Shigesawa, Multiband single-layer frequency selective surface designed by combination of genetic algorithm and geometry-refinement technique, IEEE Trans. Antennas Propag. **52,** 2925 (2004).

[60] R. Zhu, J. Wang, S. Sui, Y. Meng, T. Qiu, Y. Jia, X. Wang, Y. Han, M. Feng, L. Zheng and S. Qu, Wideband absorbing plasmonic structures via profile optimization based on genetic algorithm, Front Phys. **8,** 231 (2020).

[61] P. Y. Chen, C. H. Chen, H. Wang, J. H. Tsai, and W. X. Ni, Synthesis design of artificial magnetic metamaterials using a genetic algorithm, Opt. Express **16,** 12806 (2008).

[62] P. Ginzburg, N. Berkovitch, A. Nevet, I. Shor, and M. Orenstein, Resonances on-demand for plasmonic nano-particles, Nano Lett. **11,** 2329 (2011).

[63] R. Alaee, C. Rockstuhl, and I. Fernandez-Corbaton, An electromagnetic multipole expansion beyond the

long-wavelength approximation, Opt. Commun. **407**, 17 (2018).

[64] P. Terekhov, A. Evlyukhin, A. S. Shalin, and A. Karabchevsky, Exciting Magnetic Octupole in Near-Infrared Range by Nanostructuring, 020126, (2020).

[65] R. E. Noskov, A. Machnev, I. I. Shishkin, M. V. Novoselova, A. V. Gayer, A. A. Ezhov, E. A. Shirshin, S. V. German, I. D. Rukhlenko, S. Fleming, *et al.*, Golden vaterite as a mesoscopic metamaterial for biophotonic applications, Adv. Mater. **33**, 2008484 (2021).

[66] P. Chao, B. Strekha, R. Kuate Defo, S. Molesky, and A. W. Rodriguez, Physical limits in electromagnetism, Nat. Rev. Phys. **4**, 543 (2022).